

pubs.acs.org/cm Article

Understanding the Thermodynamic Role of Cation Substitution in P2-Na_{0.67}Mn_{0.8}M_{0.2}O₂ Cathodes via Atomistic Calculations

Shisheng Wang, Ruishan Zhang, Yanzhao Niu, Feng Pan, Wei Deng, and Bingkai Zhang*



Cite This: Chem. Mater. 2025, 37, 8226-8237



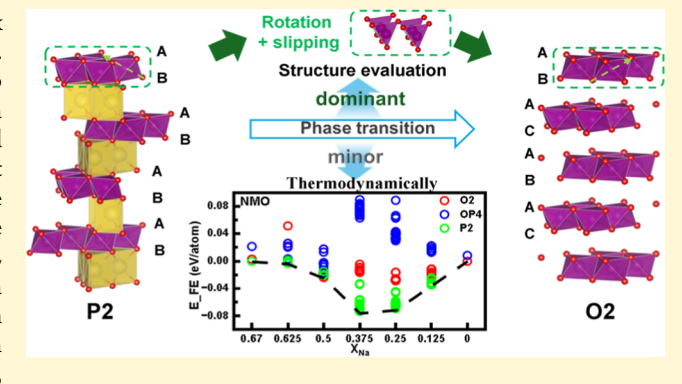
ACCESS

III Metrics & More

Article Recommendations

SI Supporting Information

ABSTRACT: P2-type $Na_{0.67}MnO_2$ cathodes suffer from complex phase transitions during cycling, limiting their practical application. In this work, first-principles calculations are employed to systematically investigate the effects of partial cation substitution in $Na_{0.67}Mn_{0.8}M_{0.2}O_2$ (M0.2-NMO) on thermodynamics, structural evolution, and phase transition evaluation. Our results reveal that cation substitution exerts only a minor influence on the thermodynamic driving forces of phase transitions owing to the marginal formation energy differences among the P2, OP4, and O2 phases. However, cation substitution has a much larger effect on structure-related factors (octahedral distortion, bond-length distortion, and shear deformation) and the tetrahedral transition states arising from MO_6 octahedral rotations and layer slipping,



suggesting that structure regulation is a more effective strategy for enhancing phase stability. Our analysis of the P2-to-O2 transition reveals that the Mg- and Co-NMO systems exhibit significantly higher barriers than pure NMO, whereas nearly all other substituted systems result in increased slipping barriers. We also investigate the effect of cation substitution on the redox mechanism during desodiation and identify the activation of oxygen redox at high states of charge. Overall, this study provides mechanistic insights into how cation substitution governs structural evolution, phase stability, and electrochemical behavior of layered sodium cathodes, offering valuable guidance for the rational design of high-performance sodium-ion battery materials.

1. INTRODUCTION

Sodium-ion batteries (SIBs) have attracted significant interest for large-scale energy storage due to the abundance and low cost of sodium, as well as their "rocking-chair" mechanism analogous to that of lithium-ion cells. 1,2 Layered transitionmetal (TM) oxides are among the most promising cathode materials, offering high reversible capacity, fast Na-ions mobility, and crystal structures similar to those of Li-ions cathodes.³ Currently, Na_{0.67}MnO₂ (NMO) compounds stand out because manganese is inexpensive and environmentally benign and its precursors are readily synthesized.^{4,5} In particular, P2-type, with a two-layer stacking, Na_{0.67}MnO₂ (P2-NMO) has been widely studied owing to its simple synthesis and excellent Na-ions conductivity due to twodimensional Na-ions diffusion channels within the P63/mmc space group. However, P2-NMO suffers from severe structural changes during repeated desodiation and sodiation processes across the TM-layers, leading to capacity fading and mechanical degradation. These issues are primarily caused by complex stacking transitions during desodiation, including P2to-OP4 and P2-to-O2 phase transformations, which induce substantial volume contraction (over 20%) and can ultimately lead to the collapse of the layers. 6-9

Cationic substitution modification (depicted in Figure S1, Supporting Information) has been proposed to address these

challenges associated with P2-NMO.¹⁰ For example, Komaba et al. systematically investigated P2-type Na_xFe_{0.5}Mn_{0.5}O₂ cathodes and revealed that reversible Fe3+/4+ redox activity and a P2 → OP4 phase transition occur during deep desodiation, as supported by in situ XRD, XAS, and Mössbauer spectroscopy. 11 Bruce et al. showed that in P2-type Na_{0.67}Mn_{0.72}Mg_{0.28}O₂, oxygen trapped in cation-induced voids is reversibly reduced during discharge, and partial reversibility of cation migration allows the high-voltage plateau to reappear upon subsequent charging.¹² Wu et al. demonstrated that the P2-type Na_{0.67}Mn_{0.89}Al_{0.11}O₂ cathode, obtained through Al incorporation, exhibits a remarkable rate capability and prolonged cycling stability.13 Wu et al. revealed the competitive interactions between Ni^{3+/4+} redox and anionic oxygen redox in P2-Na_{0.67}Li_{0.07}Mg_{0.07}Ni_{0.28}Mn_{0.58}O₂. 14 Yan et al. reported that Mg-substituted in P2-Na_{0.72}Li_{0.24}Mn_{0.76}O₂ not only reduces TM-O distances but also widens the Na-layers

Received: June 18, 2025 Revised: October 5, 2025 Accepted: October 7, 2025 Published: October 16, 2025





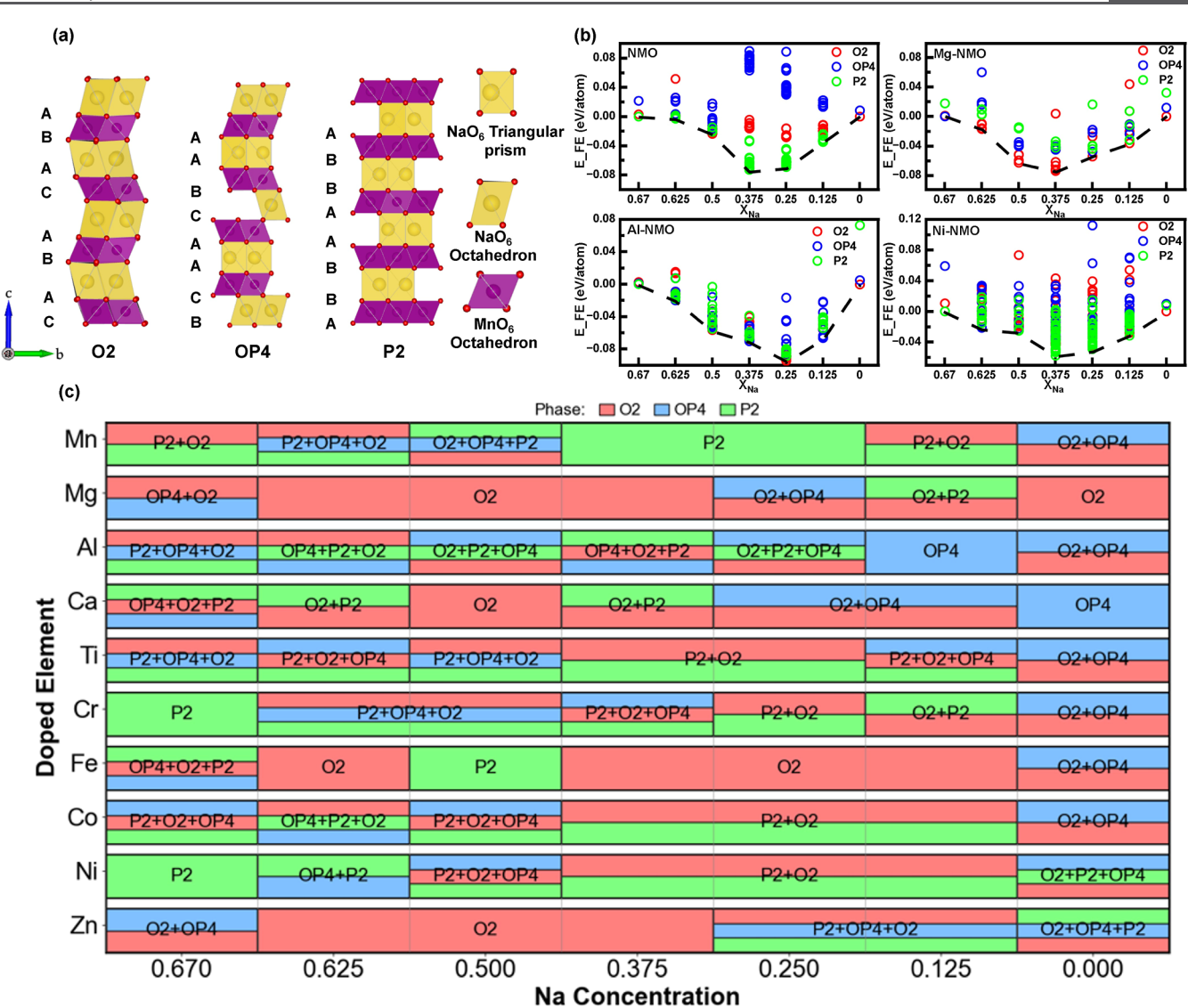


Figure 1. (a) The schematic crystal structures of the O2, OP4, and P2 phases, where the letters represent the stacking sequence of oxygen layers. (b) Formation energies of the ground-state configurations and the convex hull of representative M0.2-NMO system. (c) Phase diagram shows stable phases on the convex hull, as well as those within 0.01 eV atom⁻¹, suggesting possible phase coexistence at the same Na content. Lower positions indicate lower energy. Red, blue, and green bars represent O2, OP4, and P2 phases, respectively.

spacing, strengthening Mn 3d and O 2p orbital overlap, thus achieving reversible anionic redox and inhibiting oxygen release. Recently, Pavone et al. conducted an important theoretical investigation into the phase transition mechanisms of the P2-NMO system. They identified that local and synergistic Jahn–Teller (J–T) distortions contribute to structural instability and P2-to-O2 phase change, characterized by interlayer slip of the metal slabs and rotation of MnO6 octahedra. While most studies on cation-substituted NMO cathodes still rely on long-range or average structural characterization techniques to track phase evolution and redox reactions during electrochemical cycling, the local structures and substituent-induced interactions play a crucial role not only in enhancing electrochemical performance but also in governing degradation mechanisms. 17

To enable a comprehensive theoretical investigation of cation substitutions-induced modifications to the crystal structure, phase stability, redox mechanism, and phase transition barrier, this work employs the $Na_{0.67}Mn_{0.8}M_{0.2}O_2$ (M0.2-NMO) framework to conduct a systematic comparative

analysis of nine cation-substituted systems. Here, M represents divalent (Mg²⁺, Ca²⁺, Zn²⁺, and Ni²⁺), trivalent (Al³⁺, Cr³⁺, Fe³⁺, and Co³⁺), and tetravalent (Ti⁴⁺) ions. Thermodynamically, the desodiation-induced phase stability and electronic evolution are evaluated, and the structural evolution of the crystal lattice, including changes in Na-layer spacing, a/c ratio, octahedral distortion (D_{oct}), bond-length distortion (ρ_0), and shear fraction (η) , is examined in detail. Phase transition evaluation was performed by calculating P2-to-O2 transition pathways, including octahedral rotations and TM-layer slipping, to assess the effects of cation substitution. The roles of each substitute element in terms of thermodynamic and structural evolution effects are summarized in two tables for easy reference, respectively. In addition, the redox mechanisms and electronic structure modifications induced by different substituted cations in the M0.2-NMO system are also analyzed and summarized. Last, two four-cation substituted compounds are systematically explored to elucidate their phase transition behaviors and cooperative effects. This work elucidates the microscopic mechanisms driving phase evolution and the

influence mechanisms of substitute elements, offering both theoretical insights and practical guidance for designing highenergy-density, long-life sodium-ion battery cathodes.

2. METHODS

2.1. Theoretical Methods. All calculations were performed using density functional theory (DFT) as implemented in the Vienna Ab Initio Simulation Package (VASP), with electronic wave functions described using the projector augmented wave formulation of the generalized gradient approximation and employing the Perdew-Burke-Ernzerhof (PBE) exchange-correlation functional. ¹⁸⁻²¹ A kinetic energy cutoff of 520 eV was chosen for the plane wave basis set, with error analysis versus 720 eV presented in Figure S2. Brillouin zone sampling was conducted using a $5 \times 5 \times 1$ Monkhorst–Pack grid, which provided a reliable balance between computational efficiency and numerical precision. To properly account for magnetic and strongly correlated effects, spin-polarized calculations were performed with initial magnetic moments of 3 µB for Cr, Mn, and Fe; 1 μ B for Ni; and 0.06 μ B for all other elements. Given the significant 3d electron correlations in transition metals, the DFT + U approach²² was adopted, applying U values of 3.7 eV (Cr), 4.2 eV (Ti), 3.9 eV (Mn), 4.0 eV (Fe), 3.32 eV (Co), and 6.2 eV (Ni), respectively, while omitting U for Mg, Al, Ca, Ti, and Zn to prevent artificial localization. 23-25 Furthermore, the DFT-D3 dispersion correction scheme developed by Grimme was applied to better capture van der Waals interactions between adjacent layers.²⁶ Geometry optimizations were performed using the conjugate gradient method with convergence criteria set to 10⁻⁵ eV for electronic selfconsistency and 0.02 eV Å⁻¹ for ionic forces. The tetrahedron method with Blöchl corrections was employed to improve the accuracy of Brillouin zone integrations and to minimize entropy-related artifacts introduced by smearing, and the same settings were applied in nonself-consistent calculations.

2.2. Computational Models. The bulk structures of P2-NMO were modeled by using $2 \times 2 \times 2$ supercells containing 64 atoms to represent P2 phases (Figure 1a). The OP4- and O2-layered TM oxides share the same space group, P63mc (no. 186). In the OP4 structure, sodium alternates between prismatic and octahedral sites in adjacent layers, while in the O2 structure, sodium exclusively occupies octahedral sites. 25,27,28 Cations were introduced at Mn sites with a substitution level of 0.2, forming M0.2-NMO, using either singlecation species or multication mixtures. Considering various levels of desodiation, calculations were conducted on M0.2-NMO with the sodium content (X_{Na}) varying from 0.67 to 0 in decrements of 0.125. For the substituted and desodiated compositions, the special quasirandom structure method was used to generate all possible atomic configurations.²⁹ To reduce the computational cost, an initial screening based on Madelung energy calculations was performed across all substitution and desodiation structures, from which the ten configurations with the lowest (most negative) Madelung energies were selected for detailed structural relaxation and optimization.³

To evaluate local distortions induced by substitution, we employed the Van Vleck distortion analysis tool in pymatgen, which quantifies octahedral distortion ($D_{\rm oct}$), bond-length distortion (ρ_0), and shear fraction (η) of MnO₆ octahedra, providing a quantitative measure of symmetry perturbation. Charge redistribution effects were further investigated by mapping the magnetic moments and analyzing the projected density of states (PDOS) of the TM 3d and O 2p orbitals for each substituted system. This approach reveals how substitution modulates electronic and magnetic moments interactions, as well as underlying charge compensation mechanisms. And all phase transition tetrahedral transition states were obtained using the rmpath module implemented in USPEX. Finally, all visualizations of the crystal and electronic structures were performed using VESTA³³ and pymatgen.

The formation energies of the substituted systems were determined according to the following expression:³⁵

$$\begin{split} E_f &= [E(\text{Na}_x \text{Mn}_{0.8} \text{M}_{0.2} \text{O}_2) - \frac{x}{0.67} \times E(\text{Na}_{0.67} \text{Mn}_{0.8} \text{M}_{0.2} \text{O}_2) \\ &- \frac{0.67 - x}{0.67} \times E(\text{Mn}_{0.8} \text{M}_{0.2} \text{O}_2)] / [n(\text{atoms})] \end{split} \tag{1}$$

Here, $E(\mathrm{Na_xMn_{0.8}M_{0.2}O_2})$ is the total energy of the substituted structure at sodium content x, while $E(\mathrm{Na_{0.67}Mn_{0.8}M_{0.2}O_2})$ and $E(\mathrm{Mn_{0.8}M_{0.2}O_2})$ are the energies of the fully sodiated and fully desodiated end members, respectively. The coefficients $\frac{x}{0.67}$ and $\frac{0.67-x}{0.67}$ represent the linear mixing fractions. The result is normalized by the total number of atoms, yielding the formation energy in eV atom⁻¹. Structures within 0.01 eV atom⁻¹ of the convex hull are considered thermodynamically stable. ³⁶

The voltage of the substituted systems is calculated as

Voltage (V) =
$$\frac{E(Na_{x_2}MnO_2) - E(Na_{x_1}MnO_2) - \frac{x_2 - x_1}{2}E(Na)}{x_1 - x_2}$$
 (2)

Here, $E(Na_{x_1}Mn_{0.8}M_{0.2}O_2)$ and $E(Na_{x_2}Mn_{0.8}M_{0.2}O_2)$ are the total energies at the corresponding Na contents ($x_2 < x_1$ represent sodium concentrations), and E(Na) is the per atom energy of metallic Na, approximated as -2.61 eV.

3. RESULTS AND DISCUSSION

3.1. Thermodynamic Evaluation of Cation Effects in $Na_xMn_{0.8}M_{0.2}O_2$. First, the ground-state Na/vacancy configurations and the corresponding convex hulls derived from formation energies as a function of Na content are investigated for all ten M0.2-NMO, as shown in Figures 1b and S3. For pure NMO, the P2- and O2-type phases exhibit comparable formation energies between $X_{Na} = 0.67$ and 0.375, suggesting a thermodynamic coexistence or competition between the two structures in this intermediate regime. At X_{Na} < 0.125, the O2type phase emerges as the most stable structure. Surprisingly, the OP4 phase consistently exhibits high formation energy in the intermediate sodium content range, which not only reveals its thermodynamic instability but also implies that this phase is unlikely to form spontaneously under equilibrium conditions. Overall, for pure NMO, the phase transition initiates with the coexistence of P2 and O2, followed by stabilization of the P2 phase, and ultimately transforms into the O2 phase.

For Mg-substituted Na_xMnO₂ (Mg-NMO), we note that across the full desodiation range, the O2-type phase consistently exhibits lower formation energy than the P2 phase, indicating a thermodynamic preference for the O2 structure. These findings indicate that Mg-substitution not only stabilizes the O2-type phase thermodynamically but also promotes a balanced coexistence of the P2 and the O2 phases during desodiation, thereby enhancing structural stability. Similarly, Zn- and Ca-substituted NMO systems are also found to stabilize the O2-type phase thermodynamically. In the Al-NMO system, a persistent three-phase coexistence of P2, O2, and OP4 is maintained throughout the whole desodiation process, which is attributed to the small differences in formation energies among these phases. For the Ni-NMO system, the calculated formation energy $(-0.04 \text{ eV atom}^{-1})$ is obviously higher than pure NMO $(-0.08 \text{ eV atom}^{-1})$, relative to the two end-member reference compounds, suggesting a weaker thermodynamic driving force compared to pure NMO. As Na-ions are removed, the formation energies of the P2, O2, and OP4 phases become increasingly comparable, indicating a greater tendency for phase transitions and accelerated structural instability. Figure S4 present the ground-state

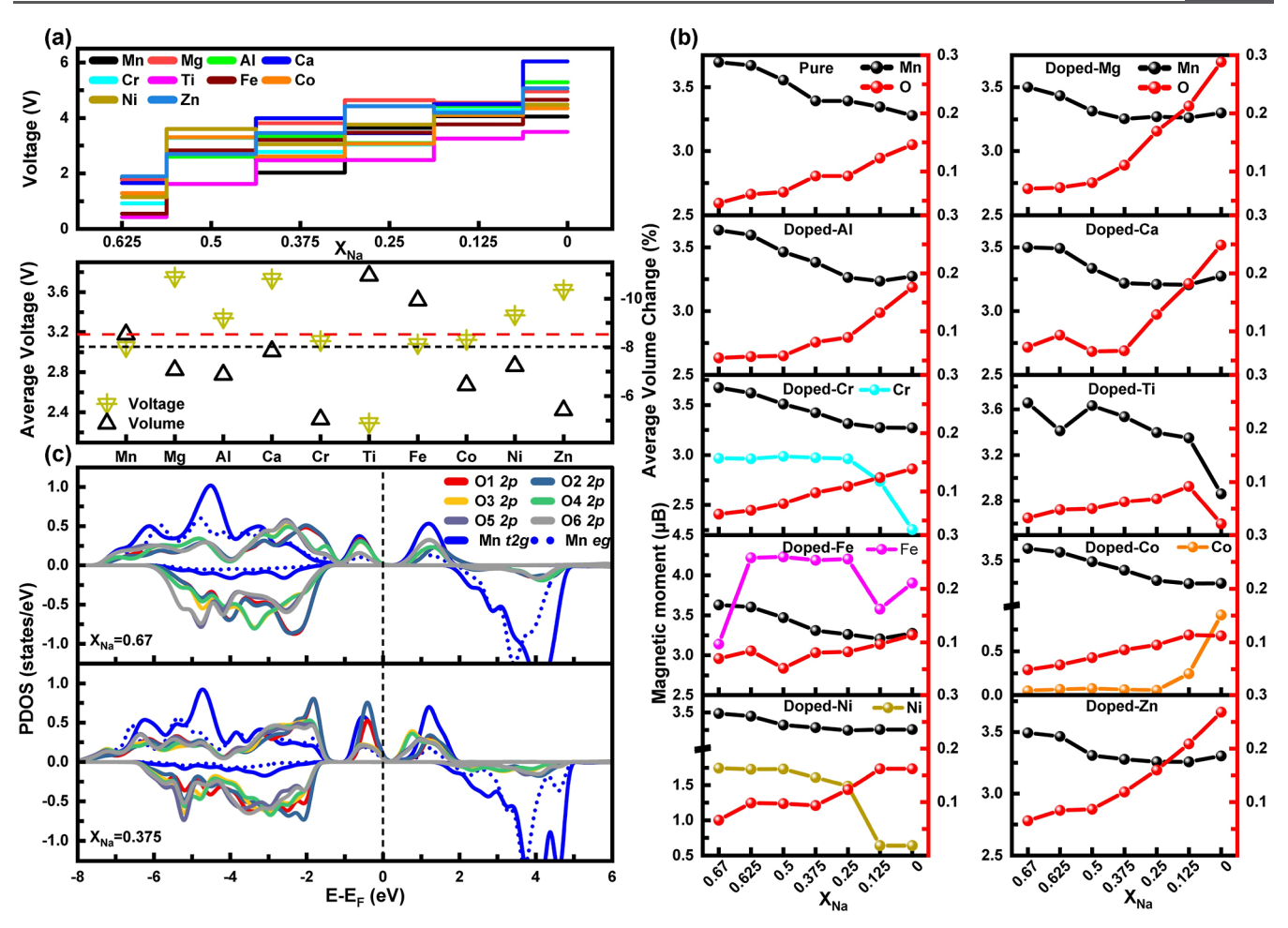


Figure 2. (a) Voltage step profiles (upper inset) and corresponding average voltages of various substituted samples (lower inset). (b) Magnetic moment variations of M and O elements with sodium content in various M0.2-NMO systems. (c) Comparison of PDOS of Mn³⁺ and its six coordinated oxygen atoms within MnO₆ octahedra at $X_{Na} = 0.67$ and 0.375, illustrating the electronic structure evolution during desodiation.

structures of the M0.2-NMO systems, where the Na-ion configurations within the Na-layers suggest a homogeneous extraction process rather than a layer-by-layer deintercalation. Figure 1c presents a comprehensive overview of the phase diagrams for M0.2-NMO systems as a function of sodium content, with phase coexistence assessed according to the criterion that structures within 0.01 eV atom⁻¹ of the convex hull are regarded as thermodynamically stable. We find that Mg-, Zn-, Ca-, and Fe-substituted NMO systems preferentially stabilize the O2-type phase during desodiation. In contrast, Ni-, Cr-, Ti-, and Co-substituted NMO systems tend to promote the formation of the OP4 phase. Furthermore, Al, Ti, Cr, and Co substituents induce multiphase coexistence, leading to more complex phase transition behaviors.

Having constructed the convex hulls of the M0.2-NMO systems, we further investigate the voltage profiles and electronic structures corresponding to each desodiation step between the identified ground states, as presented in Figure 2. Figure 2a shows the voltage profiles during desodiation, average voltage, and average volume change between $X_{\rm Na}=0.67$ and 0. The voltage steps are contributed to different redox couples and phase transformation during desodiation. To identify active redox elements during desodiation in M0.2-NMO systems, the changes in magnetic moments across sodium contents are shown in Figure 2b. For pure NMO, when $X_{\rm Na}$ falls from 0.67 to 0.375, charge compensation

primarily involves the Mn3+/4+ redox couple, corresponding to a voltage of 2.18 V. Below $X_{\text{Na}} = 0.375$, however, a pronounced rise in the oxygen magnetic moment signals the onset of the $O^{2-}/O^{(2-x)-}$ (0 < x < 1) redox process, which corresponds to the emergence of a voltage plateau around 4.0 V.^{37,38} Compared with pure NMO, substitution with Mg, Ca, and Zn induces an earlier appearance of a voltage plateau around 4.0 V. This behavior is accompanied by a pronounced increase in oxygen magnetic moments, indicating an enhanced involvement of oxygen redox processes. In the Al-NMO system, Mn magnetic moments resemble those of pure NMO, but oxygen moments rise noticeably below $X_{Na} = 0.375$, indicating the onset of oxygen redox activity. Cr-, Ni-, Co-, and Fe-substituted NMO systems actively participate in redox processes during desodiation, providing additional redox couples. Specifically, Co-, Cr-, and Ni-substituted NMO systems exhibit Co^{3+/4+}, Cr^{3+/4+}, and Ni^{2+/4+} redox couples, respectively, during deep desodiation ($X_{\text{Na}} < 0.25$). These systems also display similar $O^{2-}/O^{(2-x)-}$ redox activity to that of pure NMO; however, the presence of additional redoxactive cations contributes to an enhanced overall voltage profile. In the Fe-NMO system, as desodiation proceeds from X_{Na} = 0.375 to 0, the Fe magnetic moment gradually decreases from 4.5 to 4.0 μ B, suggesting a possible oxidation from Fe³⁺ to Fe⁴⁺. Notably, compared to pure NMO, the oxygen magnetic moment exhibits a significantly smaller increase,

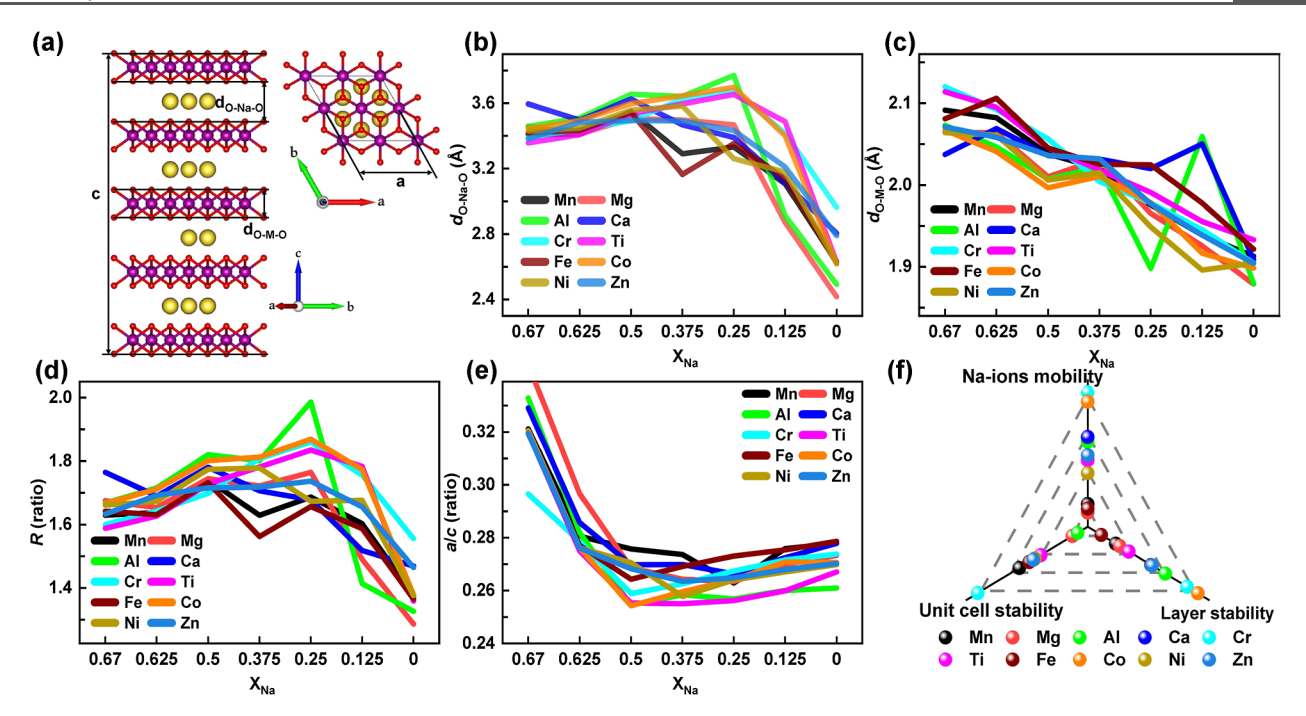


Figure 3. (a) Schematic representation of $d_{\rm O-Na-O}$ and $d_{\rm O-Ma-O}$ structural parameters. (b-e) The variations of four structural parameters during sodium extraction: the $d_{\rm O-Na-O}$, $d_{\rm O-Ma-O}$, their ratio R ($d_{\rm O-Na-O}/d_{\rm O-Ma-O}$) with the dashed reference line at R=1.62, and the lattice parameter ratio (a/c). (f) Comparative performance of different substitutes in terms of layer stability, unit cell stability, and Na-ions mobility.

indicating that oxygen redox activity is effectively suppressed in the Fe-NMO system during desodiation. For the Ti-NMO system, as the sodium content decreases from $X_{\rm Na}=0.67$ to 0.125, the Mn magnetic moment gradually decreases, while the O magnetic moment correspondingly increases. Notably, at $X_{\rm Na}=0.125$, the Mn magnetic moment suddenly drops, indicating a high-spin to low-spin transition, accompanied by a simultaneous decrease in the O magnetic moment. This behavior suggests partial charge transfer from Mn to O. The PDOS of Ti-NMO corroborates this observation: at $X_{\rm Na}=0.67$ and 0.375, the O 2p and Mn 3d orbitals partially overlap near the Fermi level, whereas at $X_{\rm Na}=0$, the Mn 3d orbital occupancy near the Fermi level is significantly higher. Together, these results indicate electron localization and charge transfer from Mn to anode O.

To further illustrate the involvement of oxygen in the redox process during desodiation, Figure 2c presents the PDOS of Mn 3d and O 2p orbitals within MnO₆ at $X_{\text{Na}} = 0.67$ and 0.375. As Na-ions are progressively extracted, the contribution of O 2p states near the valence-band maximum becomes more pronounced, accompanied by the emergence of unoccupied O 2p states close to the conduction-band minimum, indicating the formation of oxygen-hole states. Concurrently, the magnetic moments of oxygen atoms increase during desodiation, further confirming the active participation of lattice oxygen in the redox process. Similar phenomena are also observed in the Mg-, Ni-, and Fe-substituted NMO systems, as shown in Figure S5. Oxidation of transition metals to higher valence states drives O2- anions to participate in charge compensation through Mn-O interactions, resulting in the formation of $O^{(2-x)-}$ species characterized by delocalized holes. Furthermore, to assess the extent of oxygen redox in the different substituted compositions during desodiation, the variation of the O magnetic moments in M0.2-NMO from X_{Na} = 0.67 to 0 was evaluated, and the results are presented in Figure S6. It is apparent that in systems substituted with

relatively metals such as Mg, Al, Zn, and Ca, the magnetic moment variation of the O is comparatively large, indicating a higher degree of oxygen participation in the redox process. In contrast, for Cr-, Fe-, Co-, and Ni-substituted NMO systems, the presence of additional active sites reduces the relative contribution of O compared with pure NMO. Finally, in Ti-NMO, the degree of participation of O is further diminished, likely due to the electron localization and lattice distortions introduced by Ti-substitution, which enhance the involvement of Mn in charge compensation. It should be noted that oxygen redox exhibits a double-edged effect: if not properly controlled, it may cause lattice instability and accelerate structural degradation;³⁹ however, when effectively regulated, the reversible redox activity of lattice oxygen has been shown to significantly enhance capacity without compromising structural integrity, particularly in Mn-based materials. 40,41

Moreover, transition-metal migration from the TM-layers to the Na-layers is clearly identified in Mg-, Ca-, Fe-, and Zn-substituted compositions (Figures S7 and S8). For Mg-, Fe-, and Zn-NMO, the migration manifests as three elongated and three contracted M–O bonds within the octahedron. The Ca-NMO system follows a distinct pathway, with Ca-ions passing through a tetrahedral coordination at intermediate Na concentrations before stabilizing in the Na-layers. Together, these results demonstrate that partial TM migration, coupled with oxygen redox activity, stabilizes the O2 phase in Mg-, Ca-, Zn-, and Fe-substituted NMO, consistent with experimental observations.

Based on the calculated average voltages, the M0.2-NMO systems with different cations can be ranked as follows: Mg \approx Ca > Zn > Ni > Al > Co > Cr > Fe \approx Mn > Ti. The calculated voltage values corresponding to each redox couple are listed in Table S1, alongside the experimental values for comparison, showing overall consistency and thereby validating the reliability of the computational approach. From the average volume change between $X_{\rm Na} = 0.67$ and 0, a noticeable volume

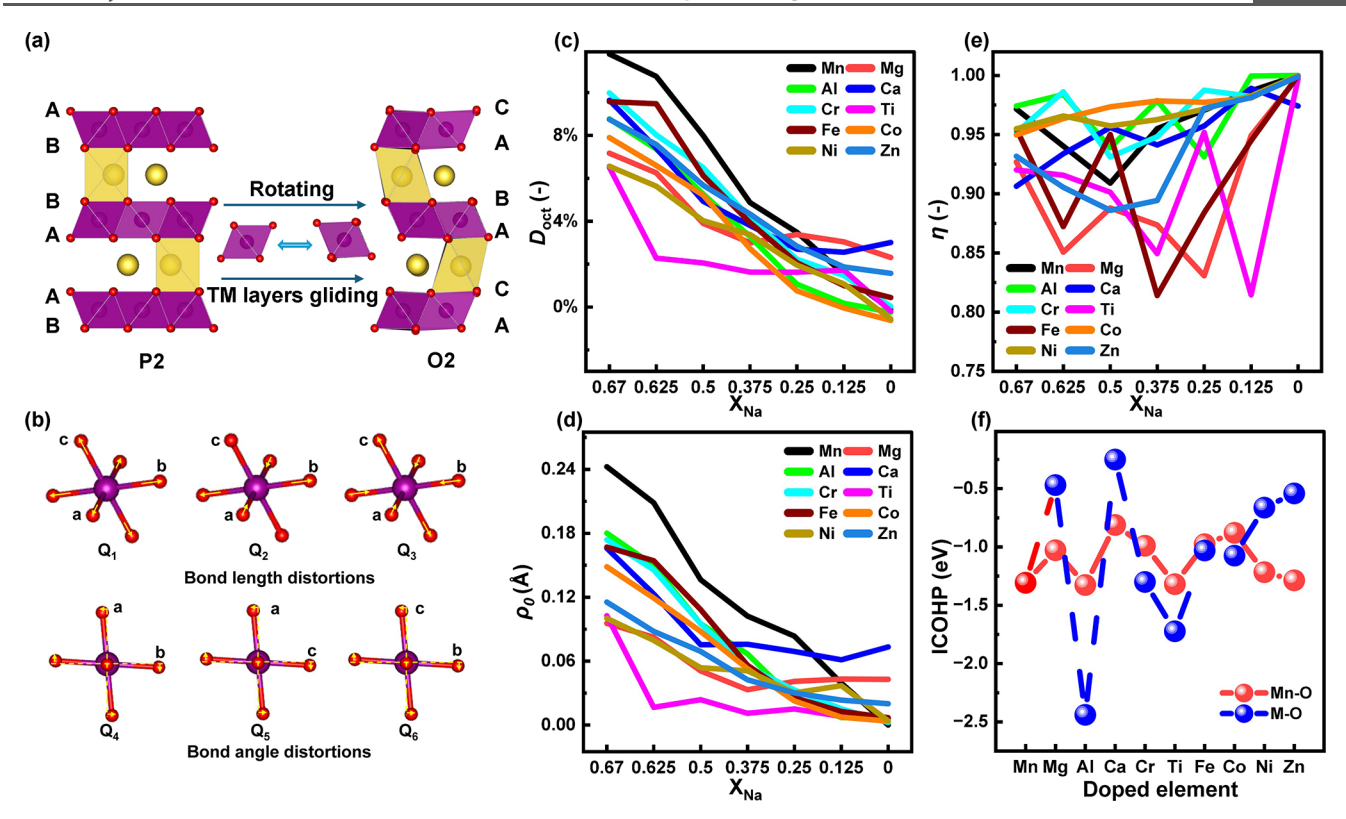


Figure 4. (a) Schematic illustration of MnO₆ rotation and TM-layer slipping during the P2-to-O2 phase transition. (b) Schematic illustration of the six Van Vleck distortion modes. (c-e) Evolution of octahedral distortion (D_{oct}), bond-length distortion (ρ_0), and shear fraction (η) of MO₆, respectively, X_{Na} from 0.67 to 0. (f) ICOHP evolution for Mn–O and M–O bonds across various substituted systems.

shrinkage is observed during desodiation. The detailed lattice parameters and cell volumes of all substituted systems are listed in Table S2. The extent of shrinkage follows the trend: Cr < Zn < Co < Al < Mg < Ni < Mn < Fe < Ti, suggesting that Cr-, Zn-, and Co-substituted NMO systems offer superior structural stability against volumetric collapse, while Fe- and Ti-substituted NMO systems are more prone to severe lattice contraction during deep desodiation. According to the calculated desodiation processes of different phases and the analysis of redox couples and volume changes, we systematically evaluated the thermodynamic effects of substitute cations on electrochemical performance, as summarized in Table S3. From the table, it is evident that cations substitution can enable the coexistence of P2 and O2 phases, as well as modulate redox potentials and structural stability. For instance, Ni, Co, and Cr substitutions exhibit a favorable balance of these effects. Mg, Al, Ca, and Zn substitutions contribute to enhanced structural stability and promote oxygen redox activity, while also mitigating volume changes during cycling. The Fe-NMO system consistently worsens all evaluated properties and is thermodynamically least desirable. Overall, from a thermodynamic perspective, cation substitution may have a limited impact on the energy differences among the three competing phases, indicating the necessity of further investigating the phase transition mechanisms from a kinetic perspective.

3.2. Structure Evaluation of M0.2-NMO during the Desodiation Process. To investigate the structure evaluation aspects governing these solid-state electrochemical phase transitions, the key structural parameters based on the desodiated structures of the O2, P2, and OP4 phases in the M0.2-NMO systems are systematically analyzed. Specifically,

we first examine the average interatomic distances within the Na-layers (d_{O-Na-O}) and the TM-layers (d_{O-M-O}) , the lattice parameter ratio (a/c), and the structural ratio R (d_{O-Na-O}) d_{O-M-O}), as shown in Figure 3a. These parameters collectively reflect the degree of lattice distortion, interlayer slipping tendency, and structural anisotropy, all of which are closely associated with phase evolution of M0.2-NMO during desodiation. 45 As shown in Figures 3b and 3c, as Na-ions are extracted, the interlayer spacing d_{O-Na-O} exhibits an initial expansion followed by contraction, whereas the d_{O-M-O} spacing decreases almost linearly with decreasing Na content. This behavior can be rationalized as follows: at the early stages of desodiation, the removal of Na-ions weakens their electrostatic shielding effect on adjacent O-ions located between the TM-layers. The resulting increase in O-O repulsion leads to an expansion of the $d_{\mathrm{O-Na-O}}$ interlayer spacing. As desodiation progresses, a delicate balance is maintained between the shielding effect of Na-ions and the repulsive interactions among O-O species. Once the balance between O–O repulsion and cationic support is disrupted, a collapse of the $d_{\rm O-Na-O}$ spacing occurs. ^{46,47} At $X_{\rm Na}$ = 0.67, the average d_{O-Na-O} interlayer spacing in pure NMO is approximately 3.408 Å. By contrast, Zn-, Ti-, and Crsubstituted NMO systems exhibit smaller initial d_{O-Na-O} values, indicating that substitutions induce the contraction of the Na-layers. Notably, during desodiation, the d_{O-Na-O} spacings in Cr- and Ti-substituted NMO systems become larger than that of pure NMO in the medium-to-high voltage region, suggesting a facilitated Na-ion migration environment. Moreover, compared with pure NMO, the evolution of $d_{\mathrm{O-Na-O}}$ as a function of Na content reveals distinct inflection points in Mg-, Co-, Ti-, and Al-substituted NMO systems

along with a delayed onset of structural contraction. These systems preserve relatively large interlayer spacings over a broader Na content range ($X_{\rm Na}=0.67-0.25$), indicating an enhanced capacity to sustain efficient ion transport even at lower sodium concentrations, prior to the onset of structural contraction. ⁴⁵

Furthermore, from the structural ratio R, $d_{\mathrm{O-Na-O}}/d_{\mathrm{O-M-O}}$, which reflects the balance between Na-layers expansion and TM-layers contraction rather than serving as a simple stability descriptor, as shown in Figure 3d, most substituted systems exhibit an increasing R value from $X_{\text{Na}} = 0.67$ to 0.5. This indicates that the expansion of the Na-layers exceeds the contraction of the TM-layers, which potentially facilitates Naions diffusion. As reported by a previous study, when R > 1.62, the P2-type layered structure becomes more stable and forms more open diffusion pathways, thereby enhancing Na-ions conductivity and cycling stability.⁴⁸ In sharp contrast, pure NMO and Fe-NMO systems maintain consistently lower R values throughout desodiation, consistent with their experimentally observed P2-to-O2 phase transitions. This behavior reflects their inferior structural stability and limited ionic transport capabilities. Notably, the Ni-, Zn-, Co-, and Crsubstituted NMO systems sustain an R value above 1.62 across a broad X_{Na} range, suggesting that these substituents broaden the Na-layers, thereby facilitating Na-ions migration and reinforcing the lattice framework. Nevertheless, it is important to underscore that structural stability requires a delicate balance of Na-layers spacing. Excessive expansion destabilizes the lattice by promoting interlayer gliding or even irreversible phase transitions, whereas excessive contraction narrows the ionic conduction channels and diminishes the Na-layers' ability to accommodate TM-layers contraction, thus accelerating unfavorable structural transformations. And as shown in Figure S9, the relative variation of the TM-layers spacing throughout the desodiation process is smaller in Ca-, Fe-, Co-, Ni-, and Znsubstituted NMO systems compared with pure NMO, which exhibits a contraction of 9.34%. This result indicates that substitution effectively suppresses TM-layer contraction, thereby contributing to enhanced structural stability during cycling. Finally, the a/c ratio is also used as an indicator of the overall unit cell anisotropic structural changes during desodiation, as shown in Figure 3e. During the initial stage of desodiation (X_{Na} > 0.5), the c-axis expands more rapidly than the a-axis, causing a sharp decline in the a/c ratio. At lower Na contents (X_{Na} < 0.5), the *c*-axis variation diminishes, and the a/c ratio stabilizes. Upon approaching full desodiation, the slight rebound of the a/c ratio arises from contraction of the c-axis parameter. Figure 3f presents a spider plot that comprehensively evaluates different cations in terms of Na-ion mobility, layer stability, and unit cell stability. Our results reveal that Ni, Zn, Co, Cr, and Al cations demonstrate overall advantages in enhancing the performance of M0.2-NMO materials.

Based on Pavone's findings, the phase transition is closely tied to the evolution of MO_6 units, involving both the TM-layers slipping and distortion-induced rotation of the MO_6 octahedra, as illustrated in Figure 4a. To this end, the Van Vleck distortion modes of the octahedral units (Figure 4b) according to the symmetry of the octahedral point group are adopted to quantify the octahedral distortion (D_{oct}), bondlength distortion (ρ_0), and shear fraction (η), as shown in Figure 4c-e. The detailed explanations and equations are provided in Section S1.1. In brief, η values approaching 1 indicate dominance of shear modes, whereas progressively

smaller η values reflect a greater contribution from bond-length distortion modes. The relative trends of η and ρ_0 also reveal that during the desodiation process, the contribution of bondlength distortion to octahedral distortion is gradually diminishing, whereas the influence of shear distortion is becoming more pronounced. At $X_{\text{Na}} = 0.67$, the pure NMO and Ti-NMO systems exhibit the highest D_{oct} , indicating the most severely distorted MO₆ geometry. Substituents such as Mg, Co, and Ni significantly reduce this distortion, enhancing structural stability. The consistent trends of ρ_0 and η with $D_{\rm oct}$ imply that both bond-length distortion and shear deformation contribute to MO₆ distortion. During desodiation, MO₆ octahedral units undergo contraction, with substituted systems typically stabilizing at ~1.93 Å M-O bond-lengths and lower distortion degrees. However, Mg-, Ca-, and Zn-substituted NMO systems retain high $D_{\rm oct}$, ρ_0 , and η values at low Na content, likely due to increasing ${\rm O^{2-}/O^{(2-x)-}}$ redox activity. Further analysis of its changes during desodiation, in pure NMO, both $D_{\rm oct}$ and ρ_0 remain high, while η rises mainly at deep Na depletion, suggesting bond-length distortion ρ_0 dominates at high Na content, and shear deformation becomes dominant as ho_0 subsides. The trend of MO $_6$ octahedral distortion shows a gradual reduction with decreasing Na content due to the increasing concentration of Mn⁴⁺ ions, which do not exhibit J-T distortion. This irregularity in shear mode contributions highlights the complex evolution of MO₆ octahedra in different chemical environments. These effects are especially pronounced in systems substituted with Fe, Ti, Zn, and Mg. Overall, these results suggest that at high sodium concentrations, D_{oct} is primarily governed by ρ_0 , while at low sodium levels, shear deformation becomes the dominant factor influencing D_{oct} , thereby shaping the overall degree of structural distortion. A more detailed analysis of Mn-O and O-O bond-length distributions is performed using the pair distribution functions (PDFs), with the results presented in Figure S10 and discussed in Section S2.1.49 To further understand the structural influence of substitute cations, the average integrated crystal orbital Hamilton population (ICOHP) of the M-O bond at $X_{\text{Na}} = 0.67$ is presented in Figure 4f. A lower ICOHP value indicates stronger M-O bonding, which is expected to effectively mitigate interlayer slipping and enhance structural integrity during electrochemical cycling. 50,51 In Al- and Ti-substituted NMO, the M-O bonds exhibit higher ICOHP values than the Mn-O bonds, reflecting a stronger covalent character of these interactions. This observation is consistent with the charge transfer and the elevated D_{oct} values seen in Ti-NMO. Enhanced covalency drives local structural rearrangements, promoting electron redistribution and resulting in pronounced distortions of the MO6 octahedra. These results indicate that cation substitution not only modifies the electronic structure but also directly affects the geometry of the transition-metaloxygen framework. In contrast, substituents such as Mg, Ca, Ni, and Zn exhibit significantly lower ICOHP values compared with Mn-O bonds, indicating weaker covalency.

In summary, to better clarify the role of cation substitutes, we summarize the structural evaluation impacts of each substitute on interlayer stability, lattice stability, and phase stability (slipping and rotation), by Na-layers spacing, R value, a/c ratio, octahedral distortion, bond-length distortion, and shear fraction, as shown in Table S4. The results suggest that Al, Cr, and Co emerge as promising substitutes for enhancing the overall electrochemical performance of pure NMO. In

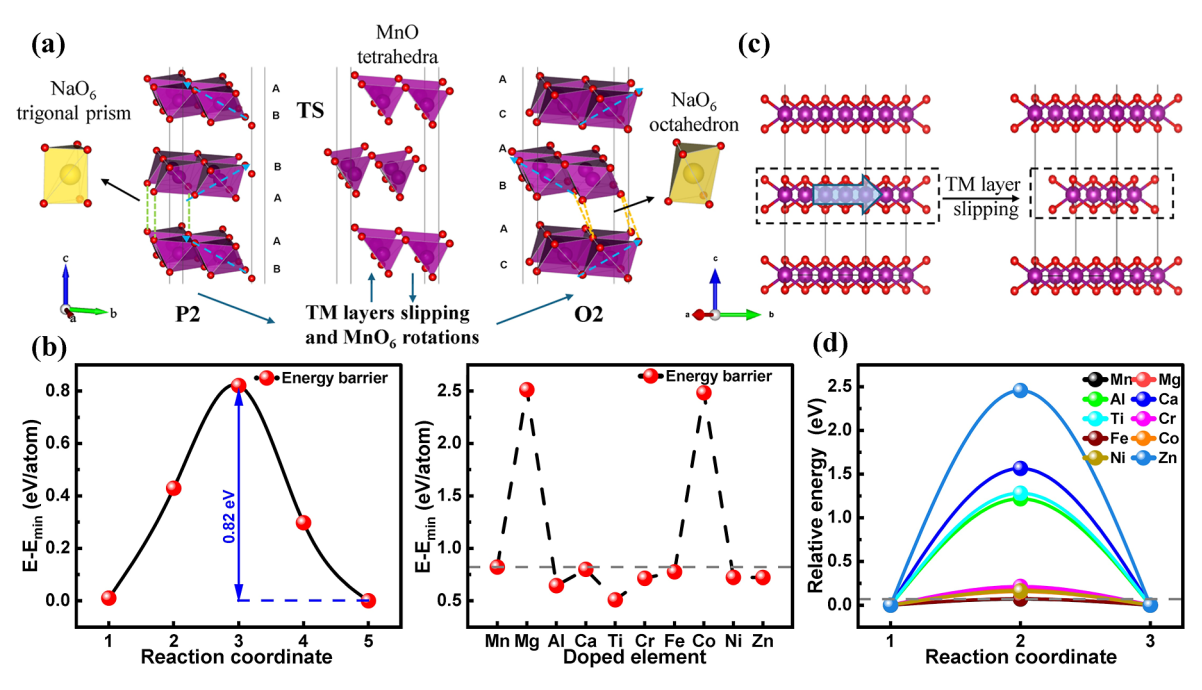


Figure 5. (a) Schematic illustration of proposed tetrahedral transition states for the P2-to-O2 phase transition, highlighting the shift of MnO_6 octahedra along the TM-layer. (b) Left: Energy profiles of the P2-to-O2 phase transition in pure NMO, coupled with MnO_6 octahedral rotations and TM-layer slipping, with barriers plotted in blue. Right: Corresponding energy barriers for the P2-to-O2 phase transition in M0.2-NMO, with the gray dashed line indicating the value for pure NMO. (c) Schematic illustration of TM-layer slipping within the ab-plane. (d) The relative energy of the M0.2-NMO structures as a function of slipping distance within the ab-plane, with the gray dashed line indicating the value for pure NMO.

contrast, Ca, Fe, Zn, and Ni may accelerate degradation and should be used with caution. Mg demonstrates mixed performance, exhibiting small values of D_{oct} , η , and ρ_0 , which suggests its potential to promote phase structural stability by suppressing interlayer slipping and MO₆ octahedral rotation. However, it also results in a small Na-layer spacing, a lower R value, and a larger a/c ratio, leading to increased unit cell stress and strain, potentially compromising long-term mechanical stability. Thus, achieving a balance between phase transition suppression and structural stability is critical.

3.3. Phase Transition Evaluation of Cation Effects in $Na_xMn_{0.8}M_{0.2}O_2$. To more directly illustrate the effect of different cation substitutions on the phase transition barrier of pure NMO, the P2-to-O2 transition state was constructed using the rmpath module in USPEX.³² The transition pathway was modeled by combining octahedral rotations with the TMlayer slipping. As illustrated schematically in Figure 5a, the octahedra within the TM-layers initially distort toward a tetrahedral-like configuration before eventually reorienting. During this process, the Na coordination environment evolves from NaO₆ prisms to NaO₆ octahedra through layer slipping. As shown in Figure 5b, the maximum P2-to-O2 phase transition barrier in pure NMO is 0.82 eV atom⁻¹, which already indicates a considerable kinetic penalty for structural rearrangement. Among the substituted systems, only Mg- and Co-substituted NMO display significantly higher barriers (~2.5 eV atom⁻¹), suggesting strong resistance to the P2-to-O2 phase transition. In contrast, all other cation-substituted systems exhibit lower barriers than pure NMO, implying that most substitutions kinetically facilitate this transition. This observation highlights the delicate role of substitutes in tuning not only the thermodynamic stability but also the kinetic accessibility of competing phases.

To further evaluate the influence of cation substitution on structural shear mechanisms, TM-layer slipping along the *ab*-axis was simulated for P2-type M0.2-NMO, as illustrated in Figure 5c. The calculated relative slipping energy change (Figure 5d) reveals that all substituted systems increase the barrier compared to pure NMO (0.07 eV). Particularly, Al-, Ti-, Zn-, and Ca-substituted systems exhibit the most pronounced enhancements, indicating a significantly reduced propensity for TM-layers slipping. The origin of this stabilization can be traced to strengthened M—O covalency, which anchors the oxygen sublattice more rigidly, as well as to the active participation of oxygen redox states, which modifies the electronic landscape and suppresses facile shear displacements.

Taken together, these results suggest a dual effect of cation substitution: (i) most substitutions lower the barrier for the P2-to-O2 transition, thereby promoting the phase transformation pathway that accommodates sodium extraction, while (ii) simultaneously increasing the resistance to undesirable TM-layer slipping events, which are typically associated with structural degradation and capacity fading. This apparent trade-off points to a design principle wherein carefully chosen dopants can accelerate favorable phase transitions while inhibiting harmful shear instabilities. In particular, elements such as Al, Ti, Zn, and Ca emerge as promising candidates for enhancing structural robustness, whereas Mg and Co may serve to suppress phase transitions altogether, potentially beneficial under high-voltage operation, where the O2 phase formation is detrimental.

Overall, the interplay between phase transition kinetics and slipping energy underscores the critical role of cation substitution in governing the structural dynamics of layered sodium transition-metal oxides. A balanced optimization of

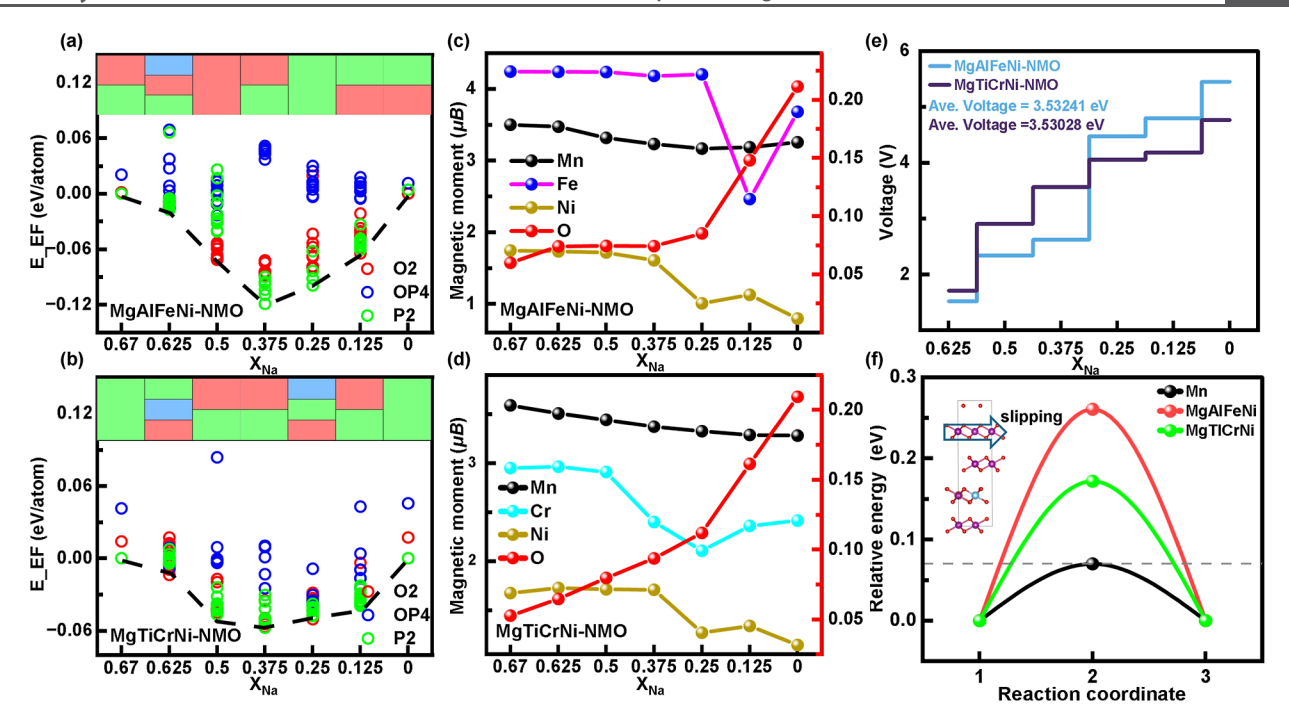


Figure 6. (a,b) show the formation energy profiles and thermal stability phase diagrams for the multication systems MgAlFeNi-NMO and MgTiCrNi-NMO, respectively. (c,d) display the evolution of magnetic moments during desodiation for each composition. (e) shows the voltage profiles for both systems. (f) shows the relative energy change for TM-layer slipping for the two systems.

these two factors may provide a pathway toward improved cycle stability and higher energy efficiency in SIBs.

3.4. Effect of Multication Substitution on Phase Stability in Na_xMn_{0.8}M_{0.2}O₂. Among the various strategies to enhance the phase stability of P2-NMO compounds, the recently explored multielement substitution has emerged as a particularly attractive approach. 52,53 To this end, two foursubstituted systems, Na_{0.67}Mg_{0.05}Al_{0.05}Mn_{0.8}Fe_{0.05}Ni_{0.05}O₂ (MgAlFeNi-NMO) and $Na_{0.67}Mg_{0.05}Ti_{0.05}Mn_{0.8}Cr_{0.05}Ni_{0.05}O_2$ (MgTiCrNi-NMO), are modeled and systematically investigated. As shown in the convex hulls (Figure 6a,b), both multication substitutions consistently reduce the baseline formation energies across various X_{Na} values compared to pure NMO. These systems predominantly exhibit coexisting P2- and O2-type phases, favoring biphasic solid-solution behavior and significantly enhancing structural phase stability. Further magnetic analysis (Figure 6c,d) reveals that the Mn magnetic moment decreases only slightly during desodiation, remaining within the range of 3.3-3.5 μ B. This indicates that the Mn^{3+/4+} redox activity is maintained, thereby maintaining electrochemical functionality, although its degree of participation is somewhat reduced. In contrast, the substituents display divergent magnetic responses during desodiation. Fe (\sim 4.3 μ B) and Cr (\sim 2.8 μ B) show high spin states at high $X_{\rm Na}$, with only minor decreases upon desodiation, indicating that they predominantly remain as Fe^{3+}/Cr^{3+} , with limited $Fe^{3+} \rightarrow Fe^{4+}$ or $Cr^{3+} \rightarrow Cr^{4+}$ transitions. Conversely, the magnetic moment of Ni (<1 μ B) drops sharply during desodiation, reflecting a sequential oxidation process from Ni²⁺ to Ni³⁺ and eventually to Ni⁴⁺. Simultaneously, the oxygen magnetic moment (red curve) increases markedly below X_{Na} < 0.375, indicating the sustained redox activity of oxygen. This signifies active oxygen redox processes that enhance charge compensation and expand the accessible capacity of SIBs. As a result, a notable voltage

enhancement is achieved, with both multication systems delivering average voltages around 3.53 V (Figure 6e). This indicates that multication substitution not only elevates the operating voltage but also fine-tunes the local crystal field and electronic structure, thereby improving structure stability. Notably, in the MgAlFeNi-NMO system at $X_{Na} = 0.125$, a pronounced migration of Mg from TM-layers to Na-layers is observed (Figure S11). This migration is primarily driven by extensive Na-ion depletion in the Na-layers under deep desodiation, which leaves numerous vacancies. Mg²⁺ ions migrate to fill these sites, mitigating local electrostatic repulsion and stabilizing the crystal structure.⁵⁴ A similar cation migration trend is observed for Ca²⁺, Zn²⁺, and Fe³⁺ ions, as shown in Figure S7. Finally, we calculated the TM-layer slipping relative energy change for both compositions (Figure 6f). The results show that the slipping energy in these substituted systems is higher than in pure NMO, indicating a reduced tendency for layer slipping. This effect partially suppresses the P2-to-OP4 or P2-to-O2 phase transitions, which are consistent with the thermodynamic observations to a certain extent. Collectively, these findings demonstrate that multication substitution at the Mn site enhances the structural stability of the P2 phase, while simultaneously improving charge compensation and supporting high-voltage output, offering a practical strategy for designing high-performance layered sodium-ion electrode materials. The lattice parameters and cell volumes of these two compositions are summarized in Table S5.

4. CONCLUSION

In this study, first-principles calculations are employed to systematically investigate the thermodynamics, structural evaluation, and effects of cation substitution in P2-type $Na_{0.67}Mn_{0.8}M_{0.2}O_2$. We first evaluated the geometric and electronic structures of M0.2-NMO across different Na

concentrations and substituent species and analyzed how each substituent influences phase transition behavior during desodiation. Thermodynamically, Mg-, Zn-, Ca-, and Fesubstituted systems tend to stabilize the O2-type phase. Ni-, Cr-, Ti-, and Co-substituted systems favor the formation of P2/O2 coexistence at low Na content. Al-, Ti-, Cr-, and Cosubstitution promote multiphase coexistence, increasing the complexity of structural evolution. Notably, Al and Ti show strong covalency with oxygen, significantly reducing the energy differences between phases and increasing the likelihood of phase coexistence. Substituents such as Mg, Al, Cr, Co, Ni, and Zn also effectively suppress volume shrinkage (within 7%), enhancing overall structural stability. During deep desodiation, the oxidized O²⁻ anions actively participate in redox processes, coupled with Mn-O interactions, forming partially oxidized $O^{(2^{-}x)-}$ species with delocalized electronic holes. This oxygen redox behavior complements the transition-metal redox couples (Ni $^{2+/4+}$, Co $^{3+/4+}$, Cr $^{3+/4+}$, and Fe $^{3+/4+}$ redox couples) and helps maintain the overall charge balance. Moreover, a correlation is observed between transition-metal migration, oxygen redox activity, and phase stability. At the same time, the stronger metal-oxygen bonding introduced by substituents can induce additional structural distortions, which may in turn promote electron localization. In Mg-, Ca-, Zn-, and Fesubstituted NMO, pronounced migration of transition-metal cations from the TM-layers to the Na-layers occurs concurrently with enhanced oxygen redox participation. Notably, in these compositions, the O2 phase exhibits greater stability compared to other competing phases. Overall, at a substitution level of M = 0.2, the thermodynamic energy differences between competing phases are relatively small, indicating that cation substitution alone has limited effect on suppressing phase transitions from a purely thermodynamic perspective. However, structure evaluation, energy barriers, and electronic structure modifications may still play a significant role in stabilizing the P2 phase.

In the structure evaluation, significant structural changes occur during desodiation, especially within the MnO₆ octahedra. In the early stages, bond-length distortions dominate, while angular shear distortions become more prominent at lower Na content. Substituents such as Mg, Ni, and Zn help mitigate these distortions, improving structural integrity. In Mg-, Co-, Ti-, and Al-substituted systems, the Nalayers spacing remains large during desodiation, facilitating Naions transport. Additionally, Ni-, Zn-, Co-, and Cr-substituted systems maintain R values $(d_{\text{O-Na-O}}/d_{\text{O-M-O}})$ above 1.62 across a broad range of Na content, indicating more stable Nalayers. In the barrier calculations, Mg- and Co-substituted systems exhibit the highest energy barriers for the overall phase transition, suggesting a certain degree of kinetic stabilization of the phase. In contrast, the evaluation of TM-layer slipping barriers reveals that nearly all substituted compositions possess higher barriers than pure NMO. Multication substitution strategies increase the average desodiation voltage, activate additional reversible redox couples, suppress J-T distortions, and mitigate phase degradation, achieving a better balance between structural stability and electrochemical performance. From a structure evaluation and energy barrier perspective, we summarize the evaluation criteria for structural evolution and phase stability: low octahedral distortion, high R value, and stable a/c ratio indicate structurally stable phases with minimal lattice deformation during cycling; high values of D_{oct} η , and ρ_0 correlate with an increased risk of layers' slipping and

structural units' rotating, which can lead to phase instability; Mg- and Co-substituted compositions exhibit a distinct kinetic advantage in maintaining phase stability compared with other substituted systems; high ICOHP values (e.g., for Ti and Al) suggest stronger M–O covalent bonding, enhancing lattice rigidity and effectively suppressing structural degradation during electrochemical cycling.

By integration of the results from thermodynamic analysis, structural evaluation, and energy barrier calculations, Al, Co, Ca, and Mg are identified as substituents with consistently strong performance across multiple aspects. In particular, Zn, Ca, and Cr demonstrate pronounced advantages in structural modification, effectively functioning as structure-stabilizing substitutions. These elements collectively contribute to balanced improvements in phase stability, thereby rendering them promising candidates for enhancing the overall electrochemical performance of the M0.2-NMO cathodes.

Moreover, our study highlights the intrinsic coupling between charge-compensation mechanisms and local structural dynamics. Specifically, octahedral distortion, bond-length variation, shear deformation, and metal—oxygen covalency are found to synergistically govern phase transition pathways and lattice stability. These insights not only deepen the fundamental understanding of structure—performance relationships but also provide practical design strategies for the development of high-performance layered cathodes for SIBs.

ASSOCIATED CONTENT

Solution Supporting Information

The Supporting Information is available free of charge at https://pubs.acs.org/doi/10.1021/acs.chemmater.5c01552.

Details of the structural evolution parameters, computational methods, and crystal structures of M0.2-NMO at various sodium contents (0.625, 0.5, 0.375, 0.25, and 0.125), together with the lowest-energy configurations, lattice constants, and selected summarized results including PDF analyses (PDF)

AUTHOR INFORMATION

Corresponding Author

Bingkai Zhang — School of Chemical Engineering and Light Industry, Guangdong University of Technology, Guangzhou 510006, China; orcid.org/0009-0008-1563-3931; Email: zhangbk@gdut.edu.cn

Authors

Shisheng Wang — School of Chemical Engineering and Light Industry, Guangdong University of Technology, Guangzhou 510006, China

Ruishan Zhang — School of Chemical Engineering and Light Industry, Guangdong University of Technology, Guangzhou 510006. China

Yanzhao Niu — School of Chemical Engineering and Light Industry, Guangdong University of Technology, Guangzhou 510006, China

Feng Pan — School of Advanced Materials, Peking University, Peking University Shenzhen Graduate School, Shenzhen 518055, China; Occid.org/0000-0002-8216-1339

Wei Deng – School of Big Data Statistics, Guizhou University of Finance and Economics, Guiyang 550025, China

Complete contact information is available at: https://pubs.acs.org/10.1021/acs.chemmater.5c01552

Notes

The authors declare no competing financial interest.

ACKNOWLEDGMENTS

This research was supported by the Natural Science Foundation of Guangdong Province (2024A1515030261), the Guangdong Key Laboratory of Design and Calculation of New Energy Materials (no. 2017B030301013), and the Guizhou Province Science and Technology Project (qiankehejichu [2024] Youth 183, qiankehezhicheng DXGA [2025] yiban014). The computations were performed on the "Guangdong University of Technology High Performance Computing Platform".

REFERENCES

- (1) Zhao, C.; Wang, Q.; Yao, Z.; Wang, J.; Sánchez-Lengeling, B.; Ding, F.; Qi, X.; Lu, Y.; Bai, X.; Li, B.; et al. Rational Design of Layered Oxide Materials for Sodium-Ion Batteries. *Science* **2020**, *370* (6517), 708–711.
- (2) Hwang, J.-Y.; Myung, S.-T.; Sun, Y.-K. Sodium-Ion Batteries: Present and Future. *Chem. Soc. Rev.* **2017**, *46* (12), 3529–3614.
- (3) Liu, Z.; Liu, R.; Xu, S.; Tian, J.; Li, J.; Li, H.; Yu, T.; Chu, S.; M. D'Angelo, A.; Pang, W. K.; et al. Achieving a Deeply Desodiated Stabilized Cathode Material by the High Entropy Strategy for Sodium-Ion Batteries. *Angew. Chem., Int. Ed.* **2024**, 63 (29), No. e202405620.
- (4) Ortiz-Vitoriano, N.; Drewett, N. E.; Gonzalo, E.; Rojo, T. High Performance Manganese-Based Layered Oxide Cathodes: Overcoming the Challenges of Sodium Ion Batteries. *Energy Environ. Sci.* **2017**, *10* (5), 1051–1074.
- (5) Liu, S.; Wang, Y.; Du, H.; Li, Y.; Wang, Y.; Wang, G.; Wang, J.; Liao, Q.; Guo, X.; Yu, H. Manganese-Based Composite-Structure Cathode Materials for Sustainable Batteries. *Adv. Energy Mater.* **2024**, 15, 2404459.
- (6) Park, Y. J.; Choi, J. U.; Jo, J. H.; Jo, C.-H.; Kim, J.; Myung, S.-T. A New Strategy to Build a High-Performance P'2-Type Cathode Material through Titanium Doping for Sodium-Ion Batteries. *Adv. Funct. Mater.* **2019**, 29 (28), 1901912.
- (7) Zuo, W.; Qiu, J.; Liu, X.; Ren, F.; Liu, H.; He, H.; Luo, C.; Li, J.; Ortiz, G. F.; Duan, H.; et al. The Stability of P2-Layered Sodium Transition Metal Oxides in Ambient Atmospheres. *Nat. Commun.* **2020**, *11* (1), 3544.
- (8) Yu, J.; Wang, D.; Wang, G.; Cui, Y.; Shi, S. Breaking the Electronic Conductivity Bottleneck of Manganese Oxide Family for High-Power Fluorinated Graphite Composite Cathode by Ligand-Field High-Dimensional Constraining Strategy. *Adv. Mater.* **2023**, 35 (8), 2209210.
- (9) Ren, M.; Zhao, S.; Gao, S.; Zhang, T.; Hou, M.; Zhang, W.; Feng, K.; Zhong, J.; Hua, W.; Indris, S.; et al. Homeostatic Solid Solution in Layered Transition-Metal Oxide Cathodes of Sodium-Ion Batteries. J. Am. Chem. Soc. 2023, 145 (1), 224–233.
- (10) Li, Y.; Zhang, T.; Song, Z.; Huang, Y.; Li, F.; Chen, A.; Li, F. Challenges and Modification Strategies on High-Voltage Layered Oxide Cathode for Sodium-Ion Batteries. *ChemSusChem* **2025**, *18* (3), No. e202401666.
- (11) Yabuuchi, N.; Kajiyama, M.; Iwatate, J.; Nishikawa, H.; Hitomi, S.; Okuyama, R.; Usui, R.; Yamada, Y.; Komaba, S. P2-Type $Na_x[Fe_{1/2}Mn_{1/2}]O_2$ Made from Earth-Abundant Elements for Rechargeable Na batteries. *Nat. Mater.* **2012**, *11* (6), 512–517.
- (12) Boivin, E.; House, R. A.; Pérez-Osorio, M. A.; Marie, J.-J.; Maitra, U.; Rees, G. J.; Bruce, P. G. Bulk O2 Formation and Mg Displacement Explain O-Redox in Na_{0.67}Mn_{0.72}Mg_{0.28}O₂. *Joule* **2021**, 5 (5), 1267–1280.
- (13) Pang, W.-L.; Zhang, X.-H.; Guo, J.-Z.; Li, J.-Y.; Yan, X.; Hou, B.-H.; Guan, H.-Y.; Wu, X.-L. P2-Type $Na_{2/3}Mn_{1.X}Al_{\chi}O_2$ Cathode Material for Sodium-Ion Batteries: Al-Doped Enhanced Electro-

- chemical Properties and Studies on the Electrode Kinetics. J. Power Sources 2017, 356, 80-88.
- (14) Huang, Z.-X.; Li, K.; Cao, J.-M.; Zhang, K.-Y.; Liu, H.-H.; Guo, J.-Z.; Liu, Y.; Wang, T.; Dai, D.; Zhang, X.-Y.; et al. New Insights into Anionic Redox in P2-Type Oxide Cathodes for Sodium-Ion Batteries. *Nano Lett.* **2024**, 24 (43), 13615–13623.
- (15) Zhang, G.; Yin, X.; Ning, D.; Chai, Y.; Du, R.; Hao, D.; Wang, C.; Liu, X.; Gao, R.; Wang, J.; et al. Crystal Modulation of Mn-Based Layered Oxide toward Long-Enduring Anionic Redox with Fast Kinetics for Sodium-Ion Batteries. *Angew. Chem., Int. Ed.* **2025**, *64* (3), No. e202415450.
- (16) Langella, A.; Massaro, A.; Muñoz-García, A. B.; Pavone, M. Atomistic Insights into Solid-State Phase Transition Mechanisms of P2-Type Layered Mn Oxides for High-Energy Na-Ion Battery Cathodes. ACS Energy Lett. 2025, 10 (3), 1089–1098.
- (17) Wang, D.; Jiao, Y.; Shi, W.; Pu, B.; Ning, F.; Yi, J.; Ren, Y.; Yu, J.; Li, Y.; Wang, H.; et al. Fundamentals and Advances of Ligand Field Theory in Understanding Structure-Electrochemical Property Relationship of Intercalation-Type Electrode Materials for Rechargeable Batteries. *Prog. Mater. Sci.* **2023**, *133*, 101055.
- (18) Kresse, G.; Furthmüller, J. Efficient Iterative Schemes for Ab Initio Total-Energy Calculations Using a Plane-Wave Basis Set. *Phys. Rev. B* **1996**, *54* (16), 11169–11186.
- (19) Kresse, G.; Furthmüller, J. Efficiency of Ab-Initio Total Energy Calculations for Metals and Semiconductors Using a Plane-Wave Basis Set. *Comput. Mater. Sci.* **1996**, *6* (1), 15–50.
- (20) Blöchl, P. E. Projector Augmented-Wave Method. *Phys. Rev. B* **1994**, *50* (24), 17953–17979.
- (21) Perdew, J. P.; Chevary, J. A.; Vosko, S. H.; Jackson, K. A.; Pederson, M. R.; Singh, D. J.; Fiolhais, C. Atoms, Molecules, Solids, and Surfaces: Applications of the Generalized Gradient Approximation for Exchange and Correlation. *Phys. Rev. B* **1992**, *46* (11), 6671–6687.
- (22) Dudarev, S. L.; Botton, G. A.; Savrasov, S. Y.; Humphreys, C. J.; Sutton, A. P. Electron-Energy-Loss Spectra and the Structural Stability of Nickel Oxide: An LSDA + U Study. *Phys. Rev. B* **1998**, *57* (3), 1505–1509.
- (23) Wang, L.; Maxisch, T.; Ceder, G. Oxidation Energies of Transition Metal Oxides within the GGA + U Framework. *Phys. Rev.* B **2006**, 73, 195107.
- (24) Jain, A.; Ong, S.; Hautier, G.; Chen, W.; Richards, W.; Dacek, S.; Cholia, S.; Gunter, D.; Skinner, D.; Ceder, G.; et al. Commentary: The Materials Project: A Materials Genome Approach to Accelerating Materials Innovation. *APL Mater.* **2013**, *1*, 011002.
- (25) Moore, G. C.; Horton, M. K.; Linscott, E.; Ganose, A. M.; Siron, M.; O'Regan, D. D.; Persson, K. A. High-Throughput Determination of Hubbard *U* and Hund *J* Values for Transition Metal Oxides Via the Linear Response Formalism. *Phys. Rev. Mater.* **2024**, *8* (1), 014409.
- (26) Grimme, S.; Antony, J.; Ehrlich, S.; Krieg, H. A Consistent and Accurate Ab Initio Parametrization of Density Functional Dispersion Correction (DFT-D) for the 94 Elements H-Pu. *J. Chem. Phys.* **2010**, 132 (15), 154104.
- (27) Lee, D. H.; Xu, J.; Meng, Y. S. An Advanced Cathode for Na-Ion Batteries with High Rate and Excellent Structural Stability. *Phys. Chem. Chem. Phys.* **2013**, *15* (9), 3304–3312.
- (28) Wang, C.; Liu, L.; Zhao, S.; Liu, Y.; Yang, Y.; Yu, H.; Lee, S.; Lee, G.-H.; Kang, Y.-M.; Liu, R.; et al. Tuning Local Chemistry of P2 Layered-Oxide Cathode for High Energy and Long Cycles of Sodium-Ion Battery. *Nat. Commun.* **2021**, *12* (1), 2256.
- (29) Zunger, A.; Wei, S. H.; Ferreira, L. G.; Bernard, J. E. Special Quasirandom Structures. *Phys. Rev. Lett.* **1990**, *65* (3), 353–356.
- (30) Madelung, E. Das Elektrische Feld in Systemen Von Regelmäßig Angeordneten Punktladungen. *Phys. Z.* **1919**, *19*, 524–533
- (31) Nagle-Cocco, L. A. V.; Dutton, S. E. Van Vleck Analysis of Angularly Distorted Octahedra Using Vanvleckcalculator. *J. Appl. Crystallogr.* **2024**, *57* (1), 20–33.

- (32) Therrien, F.; Graf, P.; Stevanović, V. Matching Crystal Structures Atom-to-Atom. J. Chem. Phys. 2020, 152 (7), 074106.
- (33) Momma, K.; Izumi, F. Vesta 3 for Three-Dimensional Visualization of Crystal, Volumetric and Morphology Data. *J. Appl. Crystallogr.* **2011**, 44 (6), 1272–1276.
- (34) Ong, S. P.; Richards, W. D.; Jain, A.; Hautier, G.; Kocher, M.; Cholia, S.; Gunter, D.; Chevrier, V. L.; Persson, K. A.; Ceder, G. Python Materials Genomics (Pymatgen): A Robust, Open-Source Python Library for Materials Analysis. *Comput. Mater. Sci.* **2013**, *68*, 314–319.
- (35) Das, H.; Urban, A.; Huang, W.; Ceder, G. First-Principles Simulation of the (Li–Ni–Vacancy)O Phase Diagram and Its Relevance for the Surface Phases in Ni-Rich Li-Ion Cathode Materials. *Chem. Mater.* **2017**, 29 (18), 7840–7851.
- (36) Sun, W.; Dacek, S. T.; Ong, S. P.; Hautier, G.; Jain, A.; Richards, W. D.; Gamst, A. C.; Persson, K. A.; Ceder, G. The Thermodynamic Scale of Inorganic Crystalline Metastability. *Sci. Adv.* **2016**, 2 (11), No. e1600225.
- (37) Dai, K.; Wu, J.; Zhuo, Z.; Li, Q.; Sallis, S.; Mao, J.; Ai, G.; Sun, C.; Li, Z.; Gent, W. E.; et al. High Reversibility of Lattice Oxygen Redox Quantified by Direct Bulk Probes of Both Anionic and Cationic Redox Reactions. *Joule* **2019**, 3 (2), 518–541.
- (38) Shadike, Z.; Zhou, Y.-N.; Chen, L.-L.; Wu, Q.; Yue, J.-L.; Zhang, N.; Yang, X.-Q.; Gu, L.; Liu, X.-S.; Shi, S.-Q.; et al. Antisite Occupation Induced Single Anionic Redox Chemistry and Structural Stabilization of Layered Sodium Chromium Sulfide. *Nat. Commun.* 2017, 8 (1), 566.
- (39) Wang, D.; Zhou, H.; Jiao, Y.; Wang, J.; Shi, W.; Pu, B.; Li, M.; Ning, F.; Ren, Y.; Yu, J. Understanding and Performance Prediction of Ions-Intercalation Electrochemistry: From Crystal Field Theory to Ligand Field Theory. *Energy Storage Science and Technology* **2022**, *11* (2), 409.
- (40) Rong, X.; Hu, E.; Lu, Y.; Meng, F.; Zhao, C.; Wang, X.; Zhang, Q.; Yu, X.; Gu, L.; Hu, Y.-S.; et al. Anionic Redox Reaction-Induced High-Capacity and Low-Strain Cathode with Suppressed Phase Transition. *Joule* **2019**, 3 (2), 503–517.
- (41) Rong, X.; Liu, J.; Hu, E.; Liu, Y.; Wang, Y.; Wu, J.; Yu, X.; Page, K.; Hu, Y.-S.; Yang, W.; et al. Structure-Induced Reversible Anionic Redox Activity in Na Layered Oxide Cathode. *Joule* **2018**, 2 (1), 125–140.
- (42) Lai, Y.; Xie, H.; Li, P.; Li, B.; Zhao, A.; Luo, L.; Jiang, Z.; Fang, Y.; Chen, S.; Ai, X.; et al. Ion-Migration Mechanism: An Overall Understanding of Anionic Redox Activity in Metal Oxide Cathodes of Li/Na-Ion Batteries. *Adv. Mater.* **2022**, *34* (47), 2206039.
- (43) Zhao, C.; Chen, C.; Hu, B.; Tong, W.; Liu, H.; Hu, B.; Li, C. Correlating Mg Displacement with Topologically Regulated Lattice Oxygen Redox in Na-Ion Layered Oxide Cathodes. *Chem. Mater.* **2022**, 34 (20), 9240–9250.
- (44) Yu, L.; Hu, C.; Wu, X.; Lou, X.; Gan, T.; Zhang, N.; Zou, Y.; Hu, B.; Li, C. Strong Correlation between Ion-Migration Generated Vacancies and Anion Redox Activity in Layered Oxides. *ACS Energy Lett.* **2025**, *10* (2), 668–677.
- (45) Kumar, B. S.; Kumar, R.; Pradeep, A.; Amardeep, A.; Srihari, V.; Poswal, H. K.; Chatterjee, A.; Mukhopadhyay, A. Fundamental Principles toward Designing High Na-Containing P2-Structured "Layered" Na-Transition Metal Oxides as High-Performance Cathode Materials for Na-Ion Batteries. *Chem. Mater.* **2022**, *34* (23), 10470–10483.
- (46) Zheng, L.; Li, J.; Obrovac, M. N. Crystal Structures and Electrochemical Performance of Air-Stable $Na_{2/3}Ni_{1/3-X}Cu_xMn_{2/3}O_2$ in Sodium Cells. *Chem. Mater.* **2017**, 29 (4), 1623–1631.
- (47) Liu, J.; Kan, W. H.; Ling, C. D. Insights into the High Voltage Layered Oxide Cathode Materials in Sodium-Ion Batteries: Structural Evolution and Anion Redox. *J. Power Sources* **2021**, *481*, 229139.
- (48) Zhao, C.; Yao, Z.; Wang, Q.; Li, H.; Wang, J.; Liu, M.; Ganapathy, S.; Lu, Y.; Cabana, J.; Li, B.; et al. Revealing High Na-Content P2-Type Layered Oxides as Advanced Sodium-Ion Cathodes. *J. Am. Chem. Soc.* **2020**, *142* (12), 5742–5750.

- (49) Terban, M. W.; Billinge, S. J. L. Structural Analysis of Molecular Materials Using the Pair Distribution Function. *Chem. Rev.* **2022**, *122* (1), 1208–1272.
- (50) Gao, S.; Zhu, Z.; Fang, H.; Feng, K.; Zhong, J.; Hou, M.; Guo, Y.; Li, F.; Zhang, W.; Ma, Z.; et al. Regulation of Coordination Chemistry for Ultrastable Layered Oxide Cathode Materials of Sodium-Ion Batteries. *Adv. Mater.* **2024**, *36* (16), 2311523.
- (51) Dronskowski, R.; Bloechl, P. E. Crystal Orbital Hamilton Populations (COHP): Energy-Resolved Visualization of Chemical Bonding in Solids Based on Density-Functional Calculations. *J. Phys. Chem.* **1993**, 97 (33), 8617–8624.
- (52) Zhao, C.; Ding, F.; Lu, Y.; Chen, L.; Hu, Y. S. High-Entropy Layered Oxide Cathodes for Sodium-Ion Batteries. *Angew. Chem., Int. Ed. Engl.* **2020**, *59* (1), 264–269.
- (53) Hu, Y.-S.; Li, Y. Unlocking Sustainable Na-Ion Batteries into Industry. ACS Energy Lett. 2021, 6 (11), 4115–4117.
- (54) Ren, H.; Li, Y.; Ni, Q.; Bai, Y.; Zhao, H.; Wu, C. Unraveling Anionic Redox for Sodium Layered Oxide Cathodes: Breakthroughs and Perspectives. *Adv. Mater.* **2022**, *34* (8), 2106171.

